Journal of Molecular Spectroscopy **210,** 51–59 (2001)
doi:10.1006/jmsp.2001.8443, available online at http://www.idealibrary.com on IDEAL®

Survey of H_3^+ Transitions between 3000 and 4200 cm^{-1}

C. Michael Lindsay, Ronald M. Rade, Jr., and Takeshi Oka

Department of Chemistry, Department of Astronomy & Astrophysics, and the Enrico Fermi Institute, The University of Chicago, 5735 S. Ellis Avenue, Chicago, Illinois, 60637

Received May 10, 2001; in revised form September 4, 2001

Most of a large gap in the laboratory rovibrational spectrum of H_3^+ between the ν_2 fundamental and the first overtone has been filled using a recently automated color center laser spectrometer which scans between 3000 and 4200 cm^{-1}. A narrow-bore liquid-nitrogen-cooled He/H_2 discharge is used to produce rotationally and vibrationally hot H_3^+. With the high-temperature plasma and the improved sensitivity of the spectrometer we were able to probe very high-energy rovibrational levels, several in the region of the barrier to linearity where theoretical calculations are expected to break down.

I. INTRODUCTION

Since its discovery in 1980 (*1*), the infrared spectrum of H_3^+ has been an important probe of H_2 dominated laboratory and astronomical plasmas. In the interstellar medium, H_3^+ has been observed in a variety of dense (*2–4*) and diffuse (*4–6*) clouds and its absorption features provide a unique measure of a cloud's temperature and column length (*3*). H_3^+ has also been detected as strong emission from the ionospheres of Jupiter (*7, 8*), Saturn (*9*), and Uranus (*10*). With high-spatial-resolution telescopes and cameras, these features are used to image the plasma activities in the Jovian ionosphere (*11*). In the laboratory, fundamental transitions of H_3^+ have been used to study nuclear spin selection rules in chemical reactions (*12*), electron recombination (*13*), the rate of ion destruction by ambipolar diffusion (*14*), and radial charge distributions in electric discharges (*15*).

The spectroscopy of H_3^+ is a rare example where the development of theoretical calculation and of experimental technique occurred simultaneously. With only three protons and two electrons, H_3^+ is theoretically tractable from first principles and is used as a benchmark for high-level rovibration calculations of polyatomic molecules (*16–18*). Despite its apparent simplicity, H_3^+ exhibits nonclassical bonding, a very anharmonic potential, and a singularity at the barrier to linearity which makes traditional coordinate systems fail at high energies. Due to these complexities, reasonable predictions of transition frequencies were only possible with high-level rovibrational calculations. Because advances in theoretical calculations occurred at the same time as the laboratory spectroscopy improved its techniques, theorists and spectroscopists worked together closely, each benefiting from the other's results. A collaboration "cycle" resulted where theorists predict transitions, spectroscopists search for, measure, and assign those transitions and theorists use the new data to improve and extend their calculations. Over the past two decades, many cycles of this interaction have been repeated and have led to the observation of over 700 transitions and the improvement in variational and *ab initio* calculations to near spectroscopic accuracy (see Ref. (*19*) for a review).

After extensive studies of the fundamental band (*20*), recent laboratory work on H_3^+ has been directed toward probing increasingly higher energy levels where the rovibrational states become badly mixed and calculations less reliable. Using difference-frequency (DF) spectrometers, earlier efforts concentrated on the region 3-4 μm where several hotbands (*21*) and high-J (*22*) transitions of the fundamental band occur. A $LiIO_3$-based DF spectrometer and diode lasers were used to probe the $2\nu_2 \leftarrow 0$ (*23*) and $3\nu_2 \leftarrow 0$ (*24*) overtone transitions. Most recently, McCall and Oka (*25*) reported $2\nu_1 + \nu_2$, the highest observed combination band so far. We refer the reader to a recent review for a summary of the previous laboratory work (*26*).

In this paper we report our continuing effort to probe higher energy states of H_3^+. Using a recently automated color center laser (CCL) spectrometer, we surveyed H_3^+ transitions from 3000 to 4200 cm^{-1} in the hottest discharge to date. With the spectrometer's significantly higher sensitivity and the plasma's higher vibrational and rotational temperatures, we were able to observe and assign 100 new transitions, several of which probe energy levels near the barrier to linearity at ~10,000 cm^{-1}.

II. EXPERIMENTAL

H_3^+ was produced in a positive column discharge and detected using velocity modulation absorption spectroscopy (*27*) (see Fig. 1). In brief, ~1 mW of 2.3- to 3.5-μm tunable radiation from a CCL was split into two beams and passed four times in opposite directions through a plasma tube in a bidirectional White cell configuration (*21*). The plasma is produced by applying ~1.7 kV (peak to peak) AC voltage with a frequency of 10 kHz across a ~1 m Pyrex tube filled with 5-Torr He and 200 mTorr H_2. The voltage was chosen to give a constant current through the tube. For this experiment, we maintained a current of 175 mA

0022-2852/01 $35.00

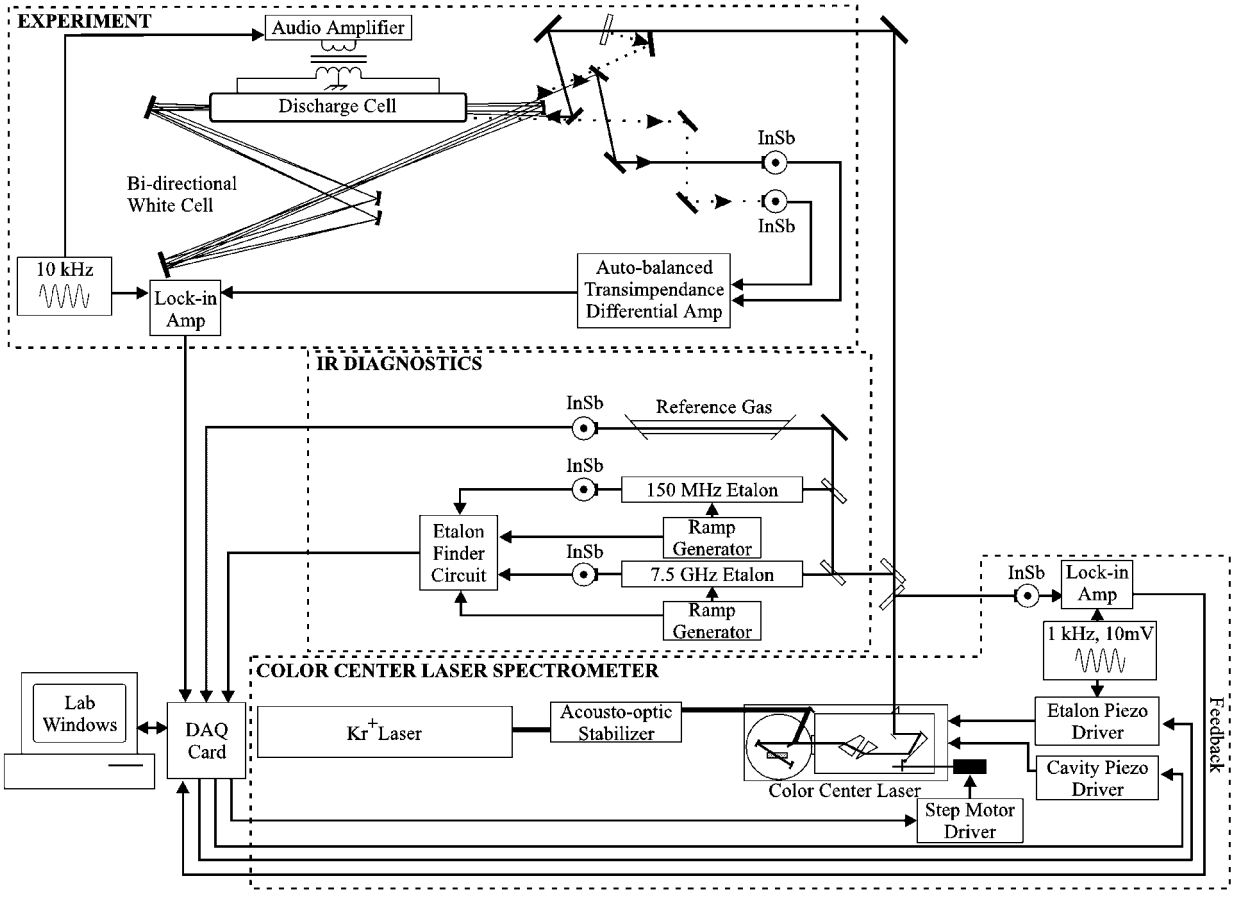

FIG. 1. Schematic diagram of the color center laser spectrometer, infrared diagnostics, and ion production/detection system.

(rms). The plasma tube, which is discussed in detail elsewhere (*14*), has more inlets than the ones used in previous H_3^+ experiments in this region but is otherwise identical. After leaving the multipass cell, the two laser beams were detected with liquid-nitrogen-cooled InSb photodiodes. The signals from these two diodes were subtracted, processed by a lock-in amplifier at the discharge frequency, and recorded by a computer. In order to avoid atmospheric water absorptions from 3600 to 4000 cm^{-1}, the entire path of the laser radiation was enclosed within acrylic boxes filled with Drierite dessicant and backfilled with dry nitrogen.

This experiment was made possible by improvements to the CCL, laser diagnostics equipment, and noise subtraction circuitry. Each of these components will now be discussed in detail.

II.1. CCL Spectrometer

Infrared radiation was produced by a Burleigh FCL-20 color center laser. Complete coverage across 3000–4200 cm^{-1} was achieved by pumping a $RbCl:Li\text{-}F_A(II)$-crystal (3000–3700 cm^{-1}) and a $KCl:Li\text{-}F_A(II)$-crystal (3700 – 4200 cm^{-1}) with 1–2.5 W of 641.7-nm single-line, multimode radiation from a Kr^+ laser (Spectra Physics Model 171). Before entering the crystal, the pump beam was sent through an acousto-optic stabilizer (Liconix Model 50SA) to decrease intensity fluctuations. The Burleigh FCL-20 is a standing wave resonator containing a lasing crystal, a low finesse scanning étalon, and a Littrow mounted grating, capable of producing a single-mode free-running bandwidth of ~1 MHz. Frequency scanning is achieved by tuning the cavity length, the étalon spacing, and the grating angle simultaneously. The commercial unit was designed to scan the cavity and étalon length together in a feedforward fashion while manually turning the grating. Full translation of the cavity mirror piezo scans the laser frequency by only 0.07 cm^{-1}. Although the étalon can be scanned ~1 cm^{-1} in a full piezo ramp, it is racheted back at the same time that the cavity rachets back due to the feedforward set-up. Consequently, this mode of operation produces very short scans without safeguards against mode-hopping and is inadequate to the study of molecules with moderate to large rotational constants.

We have overcome these problems by computer controlling each of the laser components. A number of groups have done this in the past (*28–31*, *33*), and our system is modeled after the Princeton apparatus (*33*). Two analog outputs (National Instruments Model PCI-MIO-16E-4) are amplified (Burleigh RC-44 and RC-45) and sent to the piezo translators (PZTs) attached

to a cavity folding mirror and one of the internal étalon plates. To scan the cavity resonance frequency, these two components are ramped by the computer similar to the feedforward method except that the two PZTs are racheted back individually when each piezo reaches its full extent. To minimize mode hopping during scanning or PZT rachet-backs, an error signal is produced by applying a small 1-kHz dither to the étalon PZT as discussed in Ref. (*28*). This error signal is fed back into the computer and is used to adjust the alignment of the étalon mode to the cavity mode. For faster scan rates, the étalon position is only "corrected" when the error signal is sufficiently large. The final tuning element, the grating, is attached to a 400 steps/rev stepper motor (Warner Electric Model M061-FF-206) via a 3 : 1 antibacklash, reduction gearhead (Warner Electric Model SE23-03). The driver for the stepper motor (Warner Electric Model SS2000D6) communicates digitally with the computer through three IO ports. Because the grating is a much coarser tuning element than the étalon, cavity mode hopping does not result from small misalignment of the grating and locking it to the cavity becomes unnecessary. Instead, the grating position is calibrated to the étalon position by the method introduced by Kasper *et al.* (*28*). One departure from their method is that instead of using the power of the laser as the measure of étalon-grating alignment, we use the intensity of the maximum lasing mode derived from a spectrum analyzer (see below). Controlling the laser in this way makes possible high-resolution scanning of the spectrometer over many wavenumbers at rates exceeding 10 cm^{-1}/hr.

II.2. Laser Diagnostics

While capable of covering large frequency regions with little user intervention, this method of scanning does not carefully ensure the linearity or continuity of the scanning. When the grating is stepped, the étalon and cavity PZTs are racheted back, and the cavity mode hops (this happens occasionally despite the feedback), small variations are introduced to the scanning rate. Instead of compensating for these nonlinearities in the control of the laser, we continuously monitor the frequency of the laser with a temperature stabilized 150 MHz spectrum analyzer (Burleigh CFT 500). Traditionally, the transmission of the laser through an étalon is recorded during a scan. Using the free spectral range of the étalon, the relative frequency of the laser is determined by interpolating between étalon peaks to every data point. In contrast, we ramp our étalon and record the cavity length for which a transmission occurs with the help of an "étalon finder" circuit (*32, 33*). As the laser scans, this signal takes on a sawtooth shape (see Fig. 3), hopping from one mode of the étalon cavity to the next. The étalon finder output traces the frequency of the laser and can be used to construct the relative frequency of every data point after the scan is recorded. Another, coarser, 7.5 GHz étalon (Burleigh FCL 975) is similarly monitored and is used to determine which mode the fine 150 MHz étalon is on when the laser takes a large frequency hop. The linearity of the final frequency information depends only on the stability and linearity of the 150-MHz spectrum analyzer scan between two consecutive modes. We ensured linearity by trimming the ramp drive voltage and controlling the temperature of the étalon cavity. The accuracy of the relative frequency was measured with reference gases and approaches the nominal linewidth of the laser ($\sim$0.0001 cm^{-1}).

Along with the étalon finder output, we recorded the spectra of several different reference gases. For absolute frequency calibration spectra of C_2H_4 (*34*), NH_3 (*35*), H_2O (*36*), CH_3I (*35*), C_2H_2 (*35*), and NO_2 (*37*) were used over the regions 3000–3210 cm^{-1}, 3210–3508 cm^{-1}, 3508–3895 cm^{-1}, 3895–3974 cm^{-1}, 3974–4120 cm^{-1}, and 4120–4165 cm^{-1}, respectively.

II.3. Noise Subtraction

Signal subtraction is a common technique to reduce laser intensity noise in direct absorption experiments. Double beam subtraction is particularly effective when applied to velocity modulation because both channels can be used to measure absorption when sent through an AC discharge in opposite directions. Upon subtraction, the two ion signals, which have opposite phase, effectively add together while the laser noise, spurious plasma noise, and absorption signals due to neutral molecules subtract out.

The effectiveness of this technique lies in the careful matching of the noise in the two channels before subtraction. This is generally done by manually balancing the two signals optically before detection with an optical attenuator or afterwards electronically with a voltage divider. Optimal balance is very difficult to maintain, especially during scanning due to the slight wavelength dependence of optics and étaloning within and between the optics which change the total power in each channel. Regardless of the cause, noise reduction is severely degraded when the two channels are not balanced.

Recently, P. C. D. Hobbs at IBM created a series of subtraction circuits (*38*) that automatically balance the photocurrents in a feedback-controlled current divider before subtraction. By doing this he was able to reduce amplitude fluctuations by 50–70 dB and routinely achieve shot-noise limited performance. We attempted to apply Hobbs' circuit to our InSb liquid-nitrogen-cooled photodiodes, unsuccessfully. Instead, we created a new circuit which accomplishes the same task with voltages (Fig. 2). While a detailed analysis of the circuit is left to the reader, a brief description follows.

Each photodiode is sent into a transimpedance amplifier where the photocurrents are converted to voltages, amplified, and given an offset controlled by R1 and R2. The purpose of this offset is to cancel out the background current associated with the unirradiated diode. The reference channel voltage goes through a feedback-controlled voltage divider before being subtracted from the signal voltage in Q3. A portion of the output is sent to an integrator whose result controls the voltage divider. The integrator sets the divider in such a way as to reduce the

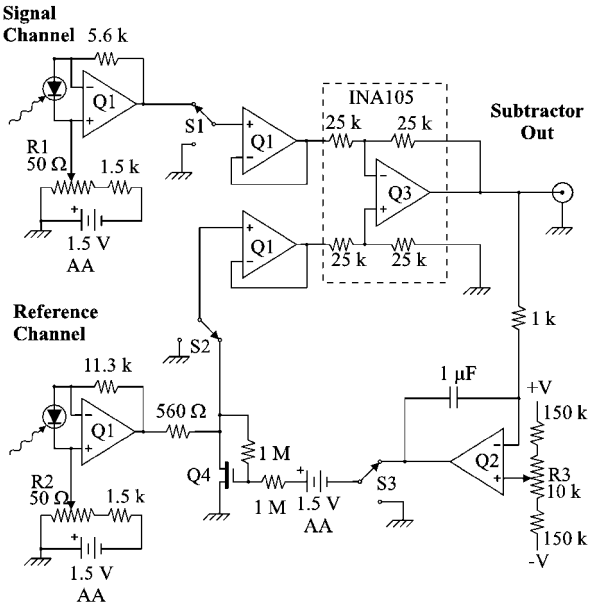

FIG. 2. Circuit diagram for the autobalancing transimpedance differential amplifier. We used the following components in our device: Q1–OP470 very low noise quad op-amp, Q2–LF356 op-amp, Q3–INA105 precision unity gain differential amplifier, and Q4–2N5457 MOSFET.

DC in the subtracted output to zero, i.e., balanced operation. In conjunction with a 10-kHz velocity modulation, this circuit decreased the noise to within a factor of 20 of the shot noise limit at a 0.3-Hz bandwidth in our system.

III. RESULTS AND DISCUSSION

We have continuously scanned for H_3^+ from 2997 to 3605 cm^{-1} and 3695 to 4165 cm^{-1} using the CCL spectrometer with a resolution (frequency between data points) of ~15 MHz. The gap from 3605–3695 cm^{-1} is due to our spectrum analyzers failing to transmit in this region, presumably because of absorption by water embedded in each étalon's fused silica optics during manufacturing. A total of 257 lines were observed and their intensities and frequencies determined by fitting each line to a Gaussian first derivative lineshape. Of these lines 101 were previously unreported and all but 6 of the lines were assigned. The transition frequencies, intensities, and assignments are listed in Table 1.

Our initial model of the H_3^+ spectrum using the calculations of Watson (*16*) and the conditions (temperature and absorption signal-to-noise ratio) reported in Bawendi *et al.* predicted ~300 new lines were observable from 3000–4200 cm^{-1}. Despite our having predicted over 75 detectable lines above 3600 cm^{-1}, the highest frequency line that we observed was at 3596.217 cm^{-1}. After assigning all of the observed lines, we performed a population distribution analysis of the discharge which revealed a much higher temperature than anticipated (more details below). The resulting increase in the partition function decreases the intensity of each transition by a factor of ~5. This is not very serious for hot bands because the increase in intensity due to the larger

TABLE 1
Observed H_3^+ Transitions and Assignments

Frequency[a] (cm^{-1})	Assignment[b]	Band[c]	Relative intensity[d]
2998.347 (15)[g]	$R(11,7)_l^l$	022←011	5.0×10^{-3}
3003.253 (05)[g]	$R(5,3)^u$	031←020	2.6×10^{-3}
3006.996 (05)[g]	$R(5,4)_l^l$	022←011	2.7×10^{-2}
3008.108 (05)[e]	$R(4,4)^u$	011←000	1.9×10^{-1}
3009.316 (05)[g]	$^tR(2,1)_l$	111←011	7.5×10^{-3}
3011.509 (05)[f]	$R(6,5)^l$	011←000	1.2×10^{-1}
3014.364 (05)[e]	$R(6,6)^l$	011←000	1.0
3015.241 (05)[e]	$R(4,3)^u$	011←000	7.8×10^{-1}
3017.628 (05)	$R(5,0)$	033←022	8.1×10^{-3}
3018.586 (05)	$R(9,8)_l$	020←011	8.8×10^{-3}
3020.495 (05)[g]	$R(4,4)$	022←011	1.6×10^{-2}
3021.862 (05)[g]	$R(6,4)_u^u$	122←111	4.7×10^{-3}
3022.424 (05)[g]	$^tR(5,1)_u^l$	111←011	8.4×10^{-3}
3023.679 (10)[g]	$R(6,3)^u$	111←100	6.5×10^{-3}
3024.439 (10)[g]	$^tR(8,5)$	100←000	8.2×10^{-3}
3024.558 (10)[e]	$R(4,2)^u$	011←000	3.5×10^{-1}
3025.941 (05)[g]	$R(7,4)^l$	011←000	1.7×10^{-2}
3026.162 (05)[g]	$^tR(6,4)$	100←000	1.5×10^{-2}
3028.543 (05)[g]	$R(8,6)_u^l$	022←011	5.7×10^{-3}
3028.977 (05)	$R(7,3)_u^l$	022←011	5.0×10^{-3}
3029.075 (10)[g]	$R(7,3)^l$	011←000	1.9×10^{-2}
3029.832 (05)[e]	$R(4,1)^u$	011←000	2.8×10^{-1}
3033.746 (05)	$R(8,3)^l$	011←000	9.5×10^{-3}
3035.475 (05)[g]	$R(4,5)$	022←011	1.1×10^{-2}
3036.720 (10)	$R(12,12)$	020←011	5.7×10^{-3}
3037.319 (05)[g]	$^tR(1,0)$	111←011	1.5×10^{-2}
3038.924 (20)[g]	$^tR(10,6)$	100←000	5.3×10^{-3}
3042.587 (10)[g]	$R(6,4)^u$	111←100	8.3×10^{-3}
3046.045 (05)[g]	$R(5,1)_l^l$	022←011	1.8×10^{-2}
3050.552 (05)[g]	$R(8,4)^l$	011←000	9.8×10^{-3}
3051.407 (05)[g]	$R(6,5)_l^l$	022←011	8.5×10^{-2}
3052.077 (05)[g]	$R(5,1)_u^u$	033←022	1.0×10^{-2}
3053.355 (05)[g]	$R(6,1)^u$	111←100	1.3×10^{-2}
3053.563 (05)[f]	$R(10,9)_l$	020←011	1.6×10^{-2}
3056.252 (00)[g]	$R(9,5)^l$	011←000	3.6×10^{-2}
3059.507 (10)[g]	$^nP(3,4)^l$	111←011	5.2×10^{-3}
3060.507 (05)[g]	$R(5,0)$	022←011	5.7×10^{-2}
3062.110 (05)	$R(6,6)^u$	111←100	7.0×10^{-3}
3062.831 (15)[g]	$^nR(0,1)$	111←011	9.1×10^{-3}
3063.101 (15)[g]	$R(11,6)^l$	011←000	1.2×10^{-2}
3063.282 (15)[g]	$R(6,3)^u$	031←020	7.5×10^{-3}
3063.935 (05)[g]	$^tR(6,2)_l^l$	111←011	1.1×10^{-2}
3064.356 (05)[f,j]	$R(7,6)^l$	011←000	2.0×10^{-1}
3064.356 (05)[j]	$R(5,2)_l^l$	022←011	2.0×10^{-1}
3065.577 (05)[g]	$R(5,2)_u^u$	022←011	4.9×10^{-2}

[a] The uncertainty in the last two digits is listed in parenthesis.

[b] We use the notation introduced by McCall (*26, 25*).

[c] Band notation corresponds to $v_1', v_2', \ell' \leftarrow v_1'', v_2'', \ell''$.

[d] The reported relative intensities are good to ±20%. The absolute intensity is only known to a factor of 5 with a value of 1.0 roughly corresponding to a peak absorption of 6×10^{-4} over a 10.8 m pathlength.

[e] First reported by Oka in Ref. (*1*).

[f] First reported by Majewski *et al.* in Ref. (*42*).

[g] First reported by Xu *et al.* in Ref. (*40*).

[h] First reported by Majewski *et al.* in Ref. (*43*).

[i] First reported by Uy *et al.* in Ref. (*22*).

[j] Overlapping lines.

TABLE 1—*Continued*

Frequency[a] (cm^{-1})	Assignment[b]	Band[c]	Relative intensity[d]
3065.777 (05)[g]	$R(5,1)_u^u$	022←011	3.4×10^{-2}
3066.565 (05)[g]	$^tR(5,3)$	100←000	9.7×10^{-3}
3067.733 (05)[g]	$R(4,2)_l^u$	022←011	1.2×10^{-2}
3069.176 (05)[f]	$R(7,7)^l$	011←000	3.3×10^{-1}
3076.175 (10)	$R(5,3)_u^u$	033←022	1.5×10^{-2}
3077.457 (10)	$^tR(6,3)$	200←100	8.3×10^{-3}
3078.892 (05)[h]	$R(9,3)^l$	011←000	1.2×10^{-2}
3085.617 (05)[g]	$^tR(5,3)_l$	111←011	5.5×10^{-2}
3086.072 (05)	$^tR(4,2)_l$	111←011	1.3×10^{-2}
3093.669 (05)[g]	$R(7,7)^u$	111←100	9.9×10^{-3}
3096.416 (05)[f]	$R(5,5)^u$	011←000	2.3×10^{-1}
3096.665 (05)[g]	$R(6,3)_l^l$	022←011	2.1×10^{-2}
3097.259 (05)[g]	$^tR(2,0)$	111←011	1.3×10^{-2}
3097.985 (05)[g]	$R(5,4)_u^u$	022←011	2.7×10^{-2}
3099.905 (05)[g]	$R(8,6)^l$	011←000	6.6×10^{-2}
3100.130 (05)	$^tR(7,3)$	200←100	7.9×10^{-3}
3100.871 (05)	$^nR(7,6)^l$	022←100	8.7×10^{-3}
3101.397 (05)[g]	$R(5,3)_u^u$	022←011	4.5×10^{-2}
3102.368 (05)[g]	$R(8,5)^l$	011←000	1.0×10^{-2}
3102.736 (05)[g]	$^tR(3,1)_l$	111←011	2.0×10^{-2}
3103.873 (05)[g]	$R(6,0)$	022←011	6.7×10^{-2}
3104.125 (10)	?	?	8.7×10^{-3}
3106.804 (05)[f]	$R(5,4)^u$	011←000	5.4×10^{-1}
3108.871 (05)	$R(7,6)_l^l$	022←011	2.0×10^{-1}
3110.877 (10)	$^nP(5,6)^l$	111←011	7.8×10^{-3}
3111.038 (10)	$^nR(9,9)$	020←100	5.2×10^{-3}
3113.532 (05)[f]	$R(8,7)^l$	011←000	1.5×10^{-1}
3115.615 (05)	$R(5,5)$	022←011	2.9×10^{-2}
3118.511 (05)[g]	$R(6,4)_l^l$	022←011	7.7×10^{-2}
3120.210 (05)[g]	$^tR(4,2)$	100←000	1.3×10^{-2}
3120.321 (05)[f]	$R(8,8)^l$	011←000	3.1×10^{-1}
3121.216 (05)[g]	$^tR(4,0)^l$	111←011	1.3×10^{-2}
3121.814 (05)[f]	$R(5,3)^u$	011←000	8.5×10^{-1}
3122.252 (05)[g]	$R(5,2)^u$	011←000	3.3×10^{-1}
3124.264 (05)	?	?	1.8×10^{-2}
3128.068 (05)[f]	$R(5,1)^u$	011←000	4.5×10^{-1}
3128.295 (05)	$R(7,2)^u$	111←100	1.4×10^{-2}
3129.516 (10)	$R(6,1)_l^l$	022←011	2.8×10^{-2}
3129.811 (05)[g]	$R(5,0)$	011←000	7.5×10^{-1}
3130.216 (05)[g]	$R(9,6)^l$	011←000	4.1×10^{-2}
3134.077 (05)	$R(7,6)^u$	031←020	1.2×10^{-2}
3136.793 (05)	$R(7,1)^u$	111←100	1.3×10^{-2}
3137.145 (05)	$R(5,6)$	022←011	4.1×10^{-2}
3137.814 (05)[g]	$R(6,3)_u^u$	022←011	1.1×10^{-1}
3138.979 (05)	$R(7,0)$	111←100	2.0×10^{-2}
3140.641 (05)[g]	$R(9,7)^l$	011←000	4.7×10^{-2}
3144.458 (05)[g]	$^tR(6,3)$	100←000	2.4×10^{-2}
3144.464 (10)[g]	$^nR(1,1)$	111←011	2.4×10^{-2}
3150.724 (05)	$R(6,1)_u^u$	022←011	3.2×10^{-2}
3151.824 (05)	$R(7,4)^u$	111←100	7.2×10^{-3}
3152.951 (05)	$R(6,2)_u^u$	022←011	3.4×10^{-2}
3159.014 (05)[g]	$R(9,8)^l$	011←000	1.1×10^{-1}
3160.236 (05)	$R(10,7)^l$	011←000	1.6×10^{-2}
3162.430 (05)	$R(10,6)^l$	011←000	7.9×10^{-3}
3163.198 (05)	$^tR(5,1)_l^l$	111←011	9.0×10^{-3}
3167.596 (05)[f]	$R(9,9)^l$	011←000	3.3×10^{-1}
3172.045 (05)	$R(8,7)_l^l$	022←011	3.7×10^{-2}
3175.189 (05)	$R(7,5)_l^l$	022←011	4.2×10^{-2}

TABLE 1—*Continued*

Frequency[a] (cm^{-1})	Assignment[b]	Band[c]	Relative intensity[d]
3177.167 (05)	$R(10,8)^l$	011←000	3.1×10^{-2}
3177.167 (05)	$R(7,3)^u$	111←100	3.1×10^{-2}
3177.628 (05)	$^nR(7,5)^u$	022←100	6.1×10^{-3}
3179.115 (05)[g]	$^tR(6,3)_l^u$	111←011	4.1×10^{-2}
3179.998 (05)[g]	$R(6,4)_u^u$	022←011	2.1×10^{-2}
3182.038 (05)[f]	$R(6,6)^u$	011←000	6.2×10^{-1}
3182.281 (05)	$^tR(5,2)_l^u$	111←011	1.3×10^{-2}
3182.605 (05)[g]	?	?	1.1×10^{-2}
3187.488 (05)	$R(11,8)^l$	011←000	1.2×10^{-2}
3188.423 (05)	$R(6,2)_l^l$	022←011	2.1×10^{-2}
3193.232 (05)[f]	$R(6,5)^u$	011←000	3.3×10^{-1}
3194.796 (05)[g]	$^tR(6,0)^l$	111←011	3.3×10^{-2}
3199.631 (05)	$^nR(7,7)^l$	022←100	1.2×10^{-2}
3200.722 (05)[g]	$R(10,9)^l$	011←000	1.2×10^{-1}
3201.386 (05)	$R(7,1)_l^l$	022←011	1.4×10^{-2}
3201.672 (05)[h]	$R(6,5)_u^u$	022←011	2.0×10^{-2}
3202.174 (05)[g]	$^tR(5,2)$	100←000	1.8×10^{-2}
3203.501 (10)[g]	$R(8,6)^u$	111←100	6.8×10^{-3}
3205.308 (05)[g]	$R(6,4)^u$	011←000	1.8×10^{-1}
3209.072 (05)[g]	$R(11,9)^l$	011←000	2.8×10^{-2}
3210.543 (05)	$R(12,9)^l$	011←000	1.0×10^{-2}
3210.801 (05)[g]	$R(10,10)^l$	011←000	9.7×10^{-2}
3212.252 (05)[f]	$R(6,2)^u$	011←000	1.2×10^{-1}
3214.612 (05)[g]	$R(6,6)$	022←011	3.5×10^{-2}
3216.360 (05)[g]	$R(6,3)^u$	011←000	2.8×10^{-1}
3219.108 (05)[g]	$^tR(7,3)$	100←000	1.2×10^{-2}
3220.181 (05)	$R(7,0)$	022←011	3.0×10^{-2}
3220.816 (05)[g]	$R(6,1)^u$	011←000	1.6×10^{-1}
3221.086 (05)	$^nQ(2,3)$	111←011	5.9×10^{-3}
3221.214 (05)	$R(7,1)_u^u$	022←011	1.9×10^{-2}
3222.022 (05)	$R(5,3)_l^u$	022←011	6.8×10^{-3}
3228.754 (05)[g]	$^tR(3,0)^u$	111←011	1.5×10^{-2}
3235.521 (05)	?	?	1.0×10^{-2}
3235.574 (05)	$R(6,7)$	022←011	1.5×10^{-2}
3235.813 (05)	$R(12,10)^l$	011←000	1.2×10^{-2}
3236.270 (05)[g]	$R(7,4)_l^l$	022←011	2.9×10^{-2}
3238.614 (05)[g]	$R(11,10)^l$	011←000	2.9×10^{-2}
3238.661 (05)[g]	$R(9,8)_l^l$	022←011	1.9×10^{-2}
3240.385 (05)[g]	$R(8,6)_l^l$	022←011	5.6×10^{-2}
3247.272 (05)	$^tR(8,2)_u^u$	111←011	1.1×10^{-2}
3247.694 (05)[g]	$R(7,2)_u^u$	022←011	1.5×10^{-2}
3247.800 (05)	$^tR(6,1)_l^l$	111←011	9.4×10^{-3}
3247.891 (05)[g]	$R(7,4)_u^u$	022←011	2.3×10^{-2}
3249.591 (05)	?	?	6.8×10^{-3}
3249.704 (05)[g]	$R(11,11)^l$	011←000	7.6×10^{-2}
3249.794 (05)[g]	$R(7,3)_u^u$	022←011	4.1×10^{-2}
3259.835 (05)[g]	$R(7,3)_l^l$	022←011	2.0×10^{-2}
3261.336 (05)	$R(8,5)_l^l$	022←011	9.9×10^{-3}
3265.138 (05)[g]	$R(7,7)^u$	011←000	9.9×10^{-2}
3265.304 (05)	$R(8,1)_u^u$	022←011	8.4×10^{-3}
3266.017 (05)[g]	$R(7,5)_u^u$	022←011	2.2×10^{-2}
3269.095 (05)	$^nR(8,5)^u$	022←100	8.2×10^{-3}
3269.496 (05)[g]	$R(8,3)^u$	111←100	8.9×10^{-3}
3270.571 (05)[g]	$R(14,12)^l$	011←000	8.3×10^{-3}
3272.713 (05)[g]	$R(12,11)^l$	011←000	2.9×10^{-2}
3276.197 (05)[g]	$R(7,6)^u$	011←000	1.4×10^{-1}
3277.429 (05)[g]	$^tR(8,3)$	100←000	1.3×10^{-2}
3282.307 (05)[g]	$^tR(6,2)$	100←000	2.7×10^{-2}

TABLE 1—*Continued*

Frequency[a] (cm^{-1})	Assignment[b]	Band[c]	Relative intensity[d]
3282.997 (05)	$^{-6}R(8,6)_u$	020←011	7.5×10^{-3}
3284.093 (05)[g]	$R(12,12)^l$	011←000	7.7×10^{-2}
3285.768 (05)[g]	$R(7,6)^u_u$	022←011	4.1×10^{-2}
3288.443 (05)[g]	$^tR(7,3)^u_l$	111←011	1.4×10^{-2}
3289.115 (05)[g]	$R(7,5)^u$	011←000	1.2×10^{-1}
3292.521 (05)[g]	$R(7,2)^l_l$	022←011	8.1×10^{-3}
3293.790 (05)[g]	$R(9,6)^u$	111←100	9.7×10^{-3}
3296.014 (05)	$R(9,9)^u$	111←100	7.6×10^{-3}
3298.990 (05)	$R(8,3)^u_u$	022←011	2.8×10^{-2}
3300.111 (10)	$^tR(5,0)^l$	111←011	6.0×10^{-3}
3301.694 (05)	$^{-6}R(8,5)_l$	020←011	9.3×10^{-3}
3302.423 (05)[i]	$R(7,4)^u$	011←000	1.0×10^{-1}
3303.093 (05)[i]	$R(13,12)^l$	011←000	2.4×10^{-2}
3305.935 (05)[i]	$R(7,1)^u$	011←000	8.0×10^{-2}
3307.150 (05)	$R(10,9)^l_l$	022←011	2.7×10^{-2}
3308.650 (10)	$R(9,7)^l_l$	022←011	2.0×10^{-2}
3308.684 (05)[i]	$R(7,0)$	011←000	5.8×10^{-2}
3309.924 (05)	$R(7,7)$	022←011	1.3×10^{-2}
3311.009 (05)	$R(8,0)$	022←011	2.2×10^{-2}
3313.752 (05)[i]	$R(13,13)^l$	011←000	3.6×10^{-2}
3317.786 (05)	$^nR(8,1)^l_u$	111←011	7.7×10^{-3}
3321.010 (05)[i]	$R(7,3)^u$	011←000	1.8×10^{-1}
3325.674 (10)	$^tR(5,1)$	100←000	7.5×10^{-3}
3328.773 (05)	$R(8,3)^l_l$	022←011	2.0×10^{-2}
3329.924 (05)[i]	$R(14,13)^l$	011←000	9.3×10^{-3}
3331.374 (05)	$R(8,4)^l_l$	022←011	1.2×10^{-2}
3331.571 (05)	$R(8,5)^u_u$	022←011	1.2×10^{-2}
3332.520 (05)	$R(7,8)$	022←011	7.3×10^{-3}
3338.534 (05)[i]	$R(14,14)^l$	011←000	1.6×10^{-2}
3343.326 (05)	$^tR(9,3)$	100←000	6.9×10^{-3}
3345.710 (05)[i]	$R(8,8)^u$	011←000	6.3×10^{-2}
3348.845 (05)	$R(9,6)^l_l$	022←011	1.6×10^{-2}
3355.517 (05)[i]	$R(8,7)^u$	011←000	6.0×10^{-2}
3356.747 (05)[i]	$R(8,2)^u$	011←000	2.7×10^{-2}
3357.525 (05)	?	?	7.6×10^{-3}
3358.400 (05)[i]	$R(15,15)^l$	011←000	1.2×10^{-2}
3362.256 (10)	$^tR(7,2)$	100←000	2.2×10^{-2}
3368.118 (05)[i]	$R(8,6)^u$	011←000	1.0×10^{-1}
3368.560 (05)	$R(8,7)^u_u$	022←011	9.7×10^{-3}
3369.664 (05)	$R(9,5)^l_l$	022←011	7.5×10^{-3}
3375.003 (05)	$R(8,6)^u_u$	022←011	2.2×10^{-2}
3376.775 (05)	$R(11,10)^u_l$	022←011	9.6×10^{-3}
3377.047 (05)	$^tR(10,3)$	100←000	8.5×10^{-3}
3380.010 (05)[i]	$R(8,5)^u$	011←000	6.5×10^{-2}
3381.399 (05)[i]	$R(8,1)^u$	011←000	4.9×10^{-2}
3388.155 (05)	$R(8,2)^l_l$	022←011	7.4×10^{-3}
3389.119 (05)	$R(9,3)^u_u$	022←011	1.1×10^{-2}
3392.547 (05)[i]	$R(8,4)^u$	011←000	4.8×10^{-2}
3395.752 (05)	$^tR(6,1)$	100←000	6.4×10^{-3}
3399.510 (05)[i]	$R(8,3)^u$	011←000	8.8×10^{-2}
3399.871 (05)	$R(8,8)$	022←011	1.1×10^{-2}
3407.501 (05)	$R(9,6)^u_u$	022←011	1.1×10^{-2}
3408.984 (10)	$R(10,7)^u_l$	022←011	5.7×10^{-3}
3411.415 (05)	$R(9,7)^u_u$	022←011	8.2×10^{-3}
3411.858 (05)[i]	$^tR(9,2)$	100←000	1.5×10^{-2}
3423.809 (05)[i]	$R(9,9)^u$	011←000	7.3×10^{-2}
3427.667 (05)	$R(8,9)$	022←011	9.3×10^{-3}
3431.295 (05)[i]	$R(9,8)^u$	011←000	6.3×10^{-2}

TABLE 1—*Continued*

Frequency[a] (cm^{-1})	Assignment[b]	Band[c]	Relative intensity[d]
3439.825 (05)	$R(11,9)^u_l$	022←011	8.4×10^{-3}
3441.416 (05)[i]	$^tR(8,2)$	100←000	2.0×10^{-2}
3443.148 (05)[i]	$R(9,7)^u$	011←000	4.4×10^{-2}
3443.466 (10)	$^tR(7,0)^l$	111←011	4.6×10^{-3}
3445.702 (05)[i]	$R(9,1)^u$	011←000	2.1×10^{-2}
3448.014 (05)	$^tR(5,0)$	100←000	6.0×10^{-3}
3450.711 (05)	$R(9,8)^u_u$	022←011	1.0×10^{-2}
3452.852 (05)[i]	$R(9,0)$	011←000	6.5×10^{-2}
3455.008 (05)[i]	$R(9,6)^u$	011←000	8.7×10^{-2}
3457.772 (05)	$^tR(10,2)$	100←000	6.7×10^{-3}
3458.383 (05)	$R(9,3)^l_l$	022←011	1.3×10^{-2}
3461.308 (05)[i]	$R(9,5)^u$	011←000	2.9×10^{-2}
3461.643 (05)	$^tR(7,1)$	100←000	5.5×10^{-3}
3473.764 (05)	$R(10,6)^u_u$	022←011	9.3×10^{-3}
3476.189 (05)[i]	$R(9,4)^u$	011←000	3.1×10^{-2}
3486.049 (05)	$R(9,9)$	022←011	7.8×10^{-3}
3497.971 (05)[i]	$R(9,3)^u$	011←000	6.1×10^{-2}
3498.764 (05)	$^{-6}R(9,5)^l$	011←000	5.3×10^{-3}
3499.417 (05)[i]	$R(10,10)^u$	011←000	2.8×10^{-2}
3503.305 (10)[i]	$R(10,9)^u$	011←000	3.3×10^{-2}
3513.541 (05)[i]	$R(10,8)^u$	011←000	2.9×10^{-2}
3516.951 (05)	$R(9,2)^u$	011←000	1.6×10^{-2}
3521.044 (05)	$R(9,10)$	022←011	4.5×10^{-3}
3523.742 (05)	$^tR(8,1)$	100←000	5.2×10^{-3}
3523.998 (05)[h]	$R(10,7)^u$	011←000	1.9×10^{-2}
3527.047 (05)	$R(10,9)^u_u$	022←011	5.9×10^{-3}
3531.279 (05)[i]	$R(10,6)^u$	011←000	4.1×10^{-2}
3546.576 (05)[i]	$R(10,5)^u$	011←000	1.1×10^{-2}
3551.579 (15)[i]	$R(10,3)^u$	011←000	1.2×10^{-2}
3552.313 (15)	$R(10,4)^u$	011←000	8.9×10^{-3}
3553.705 (15)[h]	$R(11,0)$	011←000	5.8×10^{-3}
3571.295 (15)[i]	$R(11,10)^u$	011←000	1.6×10^{-2}
3572.419 (15)[i]	$R(11,11)^u$	011←000	1.1×10^{-2}
3574.750 (15)	$^tR(7,0)$	100←000	3.5×10^{-3}
3579.301 (15)[i]	$R(11,9)^u$	011←000	1.8×10^{-2}
3586.136 (15)	$R(10,2)^u$	011←000	4.4×10^{-3}
3588.381 (15)	$R(11,8)^u$	011←000	5.9×10^{-3}
3596.217 (15)	$R(11,7)^u$	011←000	5.8×10^{-3}

Boltzmann factor overides the loss due to the higher partition function. Transitions from low energy levels, however, have only a moderate increase in their Boltzmann factor and are considerably weaker at higher temperatures. Most of the lines lying above 3600 cm^{-1} are the $2\nu_2^2 \leftarrow 0$ first overtone transitions whose intensities are affected more severely by an increase in partition function. Once the proper temperature was taken into consideration, we estimated that 10–15 detectable lines may have been missed in the gap between 3600 and 3700 cm^{-1} and that all lines above 3700 cm^{-1} were below our level of sensitivity.

Because of the high energy levels involved in the observed spectrum, assignment of transitions was only possible with the help of theoretical calculations. We found the variational calculations of Watson (*16*) and Neale, Miller, and Tennyson (NMT) (*39*), which supply both the transition intensities and frequencies

to high J level transitions, to be most useful. During our assignment process we realized that a combination of both calculations was necessary in assigning all of the lines. NMT's calculations are in general much more precise than those of Watson, usually differing from experiment by less than 0.1 cm^{-1}. For transitions involving high J levels ($J \geq 10$), however, these calculations have a serious problem and sometimes differ from the experimentally measured frequencies by as much as several cm^{-1}. For these levels Watson's calculations are more reliable. Consequently, assignments were made by a combination of the two calculations taking into account both the calculated intensities and frequencies. In a few cases we reassigned transitions that were previously reported. The assessment of previous experimental work and theoretical calculations are part of a comprehensive critical evaluation of the spectroscopic work to date which is reported in the following paper (*19*).

We have labeled the transitions following the guidelines introduced recently by McCall (*25, 26*). Accordingly, rovibrational transitions of H_3^+ are denoted by a band symbol

$$v_1' \nu_1 + v_2' \nu_2^{|\ell'|} \leftarrow v_1'' \nu_1 + v_2'' \nu_2^{|\ell''|} \qquad [1]$$

or the more compact symbol

$$v_1' v_2' |\ell'| \leftarrow v_1'' v_2'' |\ell''| \qquad [2]$$

and a branch symbol

$$^{\{n|t|\pm 6|\pm 9|\ldots\}}\{P|Q|R\}(J'', G'')^{\{u|l\}}_{\{u|l\}}, \qquad [3]$$

where v_1 and v_2 signify the number of quanta of ν_1 and ν_2 vibrational modes (when greater than 1), and ℓ is the vibrational angular momentum (understood to be zero when not present). In the branch symbol, P, Q, or R is chosen for $\Delta J = -1, 0, +1$ type transitions, respectively, directly followed by the lower state J and G values. This is preceded by a superscript specifying the change in the $G \equiv |k - \ell|$ quantum number, when $\Delta G \neq 0$. For overtone and forbidden bands ΔG can equal ± 3 (or ± 1),[1] signified by t and n respectively. For highly mixed states $|\Delta G| > 3$ are possible and these are labeled by ± 6, ± 9, etc. For states with $\ell > 0$ there are usually two ways of forming the same G for different values of k and ℓ (for example the $J = 2$ states in the ν_2 band; $k = 0$, $\ell = 1$ and $k = 2$, $\ell = 1$ both give $G = 1$). To discriminate one state from the other we associate with each G-doubled level a "u" or an "l" where the u corresponds to the higher ($u$pper) energy state and the l to the $l$ower state. This symbol is appended to our transition label as a superscript or a subscript (corresponding to the transition's upper or lower state respectively) and is left off completely for non-G-doubled states.

We assigned a total of 100 new lines in the $\nu_2 \leftarrow 0$, $\nu_1 \leftarrow 0$, $\nu_1 + \nu_2 \leftarrow \nu_1$, $\nu_1 + \nu_2 \leftarrow \nu_2$, $2\nu_2^{0,2} \leftarrow \nu_2$, $2\nu_1 \leftarrow \nu_1$, $2\nu_2^{0,2} \leftarrow \nu_1$, and $3\nu_2^{1,3} \leftarrow \nu_2^{0,2}$ bands. Many of these bands are forbidden transitions (*40*) that become observable by intensity borrowing from allowed transitions. Figure 3 shows an example scan of a 5-Torr He/200 mTorr H_2 discharge. In addition to the H_3^+ lines, we can see in this sample a transition from NH_3^+. Impurities within the reagent gases can give rise to large absorption signals from ions other than H_3^+. These impurity signals are easily identified by their narrower linewidth and known transition frequencies. Every strong H_3^+ line was assigned to a predicted transition except for only one case where two lines ($\nu_2 \leftarrow 0$, $R(7, 6)^l$ and $2\nu_2^2 \leftarrow \nu_2$, $R(5, 2)_l^l$) were calculated to be close to one another and we assumed that they overlap to form a single observable feature. We were unable to assign six weak (signal-to-noise ratio <4) cation absorption features attributed to H_3^+ based on their large line width and lack of frequency correspondence to any known impurity ion. It is possible that these transitions probe levels above the barrier to linearity where the calculations are expected to be breakdown, explaining why no reasonable match could be found. Until an assignment is made, however, the identity of the carrier of each of these features remains in question.

Most of the new transitions are due to higher rotational states of hot bands. There are several transitions whose lower states are from levels with two quanta of vibrational excitation, allowing us to probe triply excited states. Overall, 60 transitions probed states above 8000 cm^{-1}, 16 of these between 9000 and 10,000 cm^{-1}, and one above 10,000 cm^{-1}. The potential barrier to linearity is calculated to be ~9900 cm^{-1} above the zero point energy (*41*), and these transitions offer the best experimental test yet of *ab initio* calculations in this computationally difficult region. A detailed comparison of this and all previous experimental studies has been performed by Lindsay and McCall and is reported in the following paper (*19*).

Because this survey encompassed a wide variety of transitions and was measured on a spectrometer with relatively stable power, we were able to perform for the first time a complete population analysis of H_3^+ over a large number of rotational and vibrational states. Molecules in electric discharges are not in thermal equilibrium but can often be characterized as having Boltzmann distributions within each degree of freedom. Allowing for a different distribution between rotational and vibrational states, we can write an expression for the absorption intensity (for weak absorptions),

$$I_{\text{exp}} = A(2J + 1)\, g S e^{\frac{-E''_{\text{rot}}}{kT_{\text{rot}}}} e^{\frac{-E''_{\text{vib}}}{kT_{\text{vib}}}}, \qquad [4]$$

where A is a constant of proportionality, and g is the statistical weight of the nuclear spin modifications ($g = 4$ for $I = 3/2$,

[1] This "rule" is somewhat misleading and deserves more explanation. The signed G, denoted $g \equiv k - \ell$, carries the selection rule $\Delta g = 0, \pm 3, \pm 6, \ldots$ due to the parity and nuclear spin selection rules. The confusion begins when g goes from a positive to a negative value or vice versa. Take for example an overtone transition where $k'' = \pm 1$, $\ell'' = 0$ and $k' = 0$, $\ell' = \pm 2$. In this case $g'' = \pm 1$, $g' = \mp 2$, $G'' = 1$, and $G' = 2$. The transition $\Delta g = \mp 3$ is clearly allowed but ΔG appears to be a misleading $+1$. Both transitions are properly labeled with an n; a label of t would denote the transition $g'' = \pm 1$ to $g' = \pm 4$, where $\Delta g = \pm 3$ and $\Delta G = +3$.

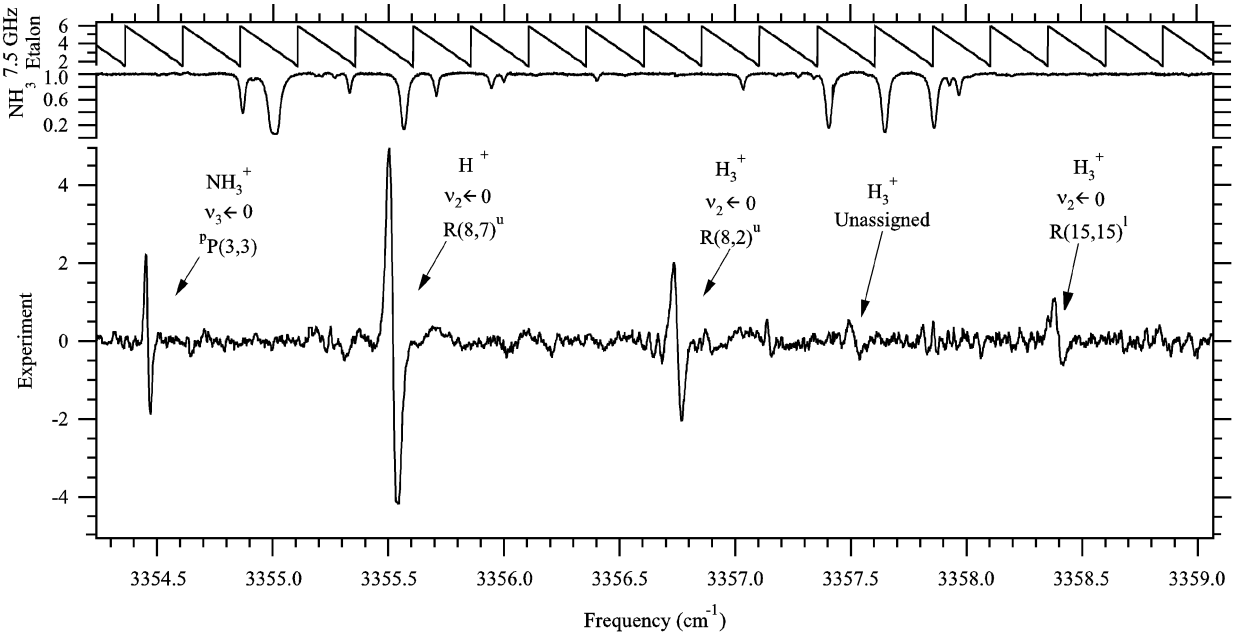

FIG. 3. An example scan of a 5 Torr He/200 mTorr H_2 discharge. Impurities in the reagent gases give rise to strong absorption signals from ions other than H_3^+. These signals are easily identified by their narrower linewidth and known transition frequencies.

ortho-H_3^+ and $g = 2$ for $I = 1/2$, *para*-H_3^+), and S is the transition strength. For H_3^+ the states are very mixed and Hönl–London factors cannot adequately describe the intensity. Instead, we used S from Watson's calculated linestrengths (the intensities in NMT's calculation were equally good). We also used the calculated values of the lower state rotational and vibrational energies, E''_{rot} and E''_{vib} in Watson's table. Rewriting expression [4] in terms of E''_{rot} and E''_{vib}, we get

$$\ln\left(\frac{I_{\text{exp}}}{(2J+1)\,gS}\right) = \ln A - \frac{1}{kT_{\text{rot}}}E''_{\text{rot}} - \frac{1}{kT_{\text{vib}}}E''_{\text{vib}}. \quad [5]$$

A least-squares regression of the left side of this equation versus E_{rot} and E_{vib} gives us a rotational temperature of 1137 ± 10 K and a vibrational temperature of 1769 ± 10 K. This fit has been depicted as two separate Boltzmann plots in Fig. 4.

It is clear from these diagrams that in our discharge the rotational and vibrational populations are internally thermalized. This sharply contradicts the results in Bawendi *et al.* (*21*) which observed different rotational temperatures in the ground and ν_2 state as well as a substantial population inversion between the ν_1 and ν_2 vibrational states. In their calculations, a total of 10 transitions of low J value were used to determine all 4 temperatures. Furthermore, each was determined by comparing transitions between closely spaced levels, some only a couple of hundred wavenumbers apart. Our temperature calculations included hundreds of lines scattered across thousands of wavenumbers giving a much more reliable determination of the H_3^+ population distribution. It appears that prospects for using H_3^+ as a laser source, as suggested by Bawendi *et al.*, are poor.

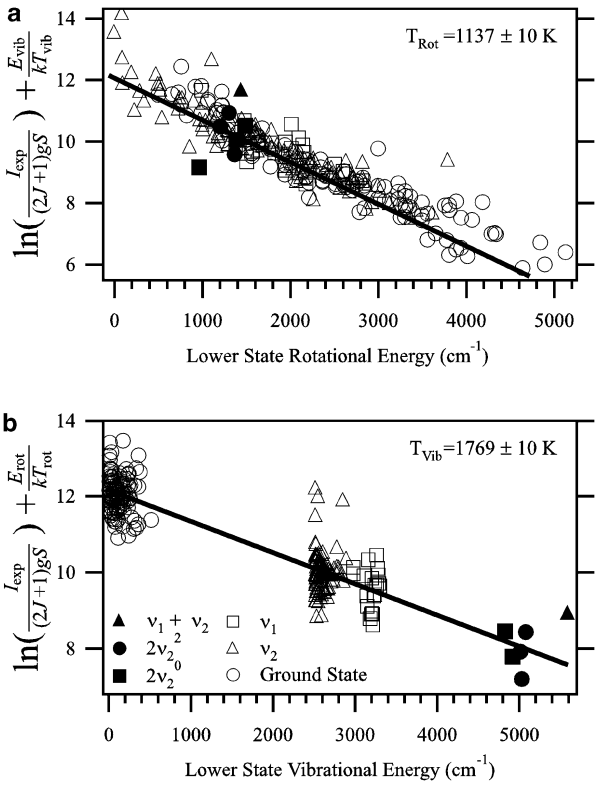

FIG. 4. Two-dimensional representations of (a) rotational and (b) vibrational Boltzmann plots. The vibrational and rotational temperatures were determined simultaneously in a multivariate least-squares fit. It is clear from these plots that H_3^+ in this discharge is well thermalized within each type of motion.

IV. CONCLUSION

The increase in sensitivity of the spectrometer compared to earlier work in this region allowed us to take advantage of this very hot discharge, increasing the number high rotational and vibrational H_3^+ states that have been probed experimentally. This work substantially expands the list of experimentally measured rovibrational states to high energy, providing an important tool for theorists who use H_3^+ as a benchmark for rovibrational calculations for other molecular systems. It appears that we have finally entered the regime of the barrier to linearity. While the ultimate test of *ab initio* rovibrational calculations is to excite H_3^+ into a vibrational state above the barrier, some of the states probed in this work reach vibrational energies of $\sim$8500 cm^{-1}—possibly high enough to begin to observe the effects of the linearity problem in some calculations.

ACKNOWLEDGMENTS

We thank E. R. T. Kirstal, A. Callegari, and K. K. Lehmann for their help in the development of the CCL spectrometer. We also thank J. K. G. Watson and J. Tennyson for supplying us with transition calculations and for the discussion of theory. P. Hobbs's advice on autosubtraction is also appreciated. We acknowledge K. Arai for his assistance in developing the autosubtractor and B. J. McCall for many helpful discussions of H_3^+. This work was supported by NSF Grant PHY-9722691 and NASA Grant NAG5-9583.

REFERENCES

1. T. Oka, *Phys. Rev. Lett.* **45,** 531–534 (1980).
2. T. R. Geballe and T. Oka, *Nature* **384,** 334–335 (1996).
3. B. J. McCall, T. R. Geballe, K. H. Hinkle, and T. Oka, *Astrophys. J.* **522,** 338–348 (1999).
4. B. J. McCall, K. H. Hinkle, T. R. Geballe, and T. Oka, *Faraday Discuss.* **109,** 267–280 (1998).
5. B. J. McCall, T. R. Geballe, K. H. Hinkle, and T. Oka, *Science* **279,** 1910–1912 (1989).
6. T. R. Geballe, B. J. McCall, K. H. Hinkle, and T. Oka, *Astrophys. J.* **510,** 251–257 (1999).
7. P. Drossart, J.-P. Maillard, J. Caldwell, S. J. Kim, J. K. G. Watson, W. A. Majewski, J. Tennyson, S. Miller, S. K. Atreya, J. T. Clarke, J. H. Waite, Jr., and R. Wagener, *Nature* **340,** 539–541 (1989).
8. L. Trafton, D. F. Lester, and K. L. Thompson, *Astrophys. J.* **343,** L73–76 (1989).
9. T. R. Geballe, M. F. Jagod, and T. Oka, *Astrophys. J.* **408,** L109–112 (1993).
10. L. M. Trafton, T. R. Geballe, S. Miller, J. Tennyson, and G. E. Ballester, *Astrophys. J.* **405,** 761–766 (1993).
11. J. E. P. Connerney and T. Satoh, *Philos. Trans. R. Soc. London* **358,** 2471–2483 (2000).
12. M. Cordonnier, D. Uy, R. M. Dickson, K. E. Kerr, Y. Zhang, and T. Oka, *J. Chem. Phys.* **113,** 3181–3193 (2000).
13. T. Amano, *Astrophys. J.* **329,** L121–124 (1988).
14. C. M. Lindsay, E. T. White, and T. Oka, *Chem. Phys. Lett.* **328,** 129–134 (2000).
15. F.-S. Pan and T. Oka, *Phys. Rev. A* **36,** 2297–2310 (1987).
16. J. K. G. Watson, *Chem. Phys.* **190,** 291–300 (1995).
17. R. Jaquet, W. Chencek, W. Kutzelnigg, and J. Rychlewski, *J. Chem. Phys.* **108,** 2837–2846 (1998).
18. O. L. Polyansky and J. Tennyson, *J. Chem. Phys.* **110,** 5056–5064 (1999).
19. C. M. Lindsay and B. J. McCall, *J. Mol. Spectrosc.* **210,** 60–83 (2001).
20. J. K. G. Watson, S. C. Foster, A. R. W. McKellar, P. Bernath, T. Amano, F. S. Pan, M. W. Crofton, R. S. Altman, and T. Oka, *Can. J. Phys.* **62,** 1875–1885 (1984).
21. M. G. Bawendi, B. D. Rehfuss, and T. Oka, *J. Chem. Phys.* **93,** 6200–6209 (1990).
22. D. Uy, C. M. Gabrys, M.-F. Jagod, and T. Oka, *J. Chem. Phys.* **100,** 6267–6274 (1994).
23. L.-W. Xu, C. M. Gabrys, and T. Oka, *J. Chem. Phys.* **93,** 6210–6215 (1990).
24. S. S. Lee, B. F. Ventrudo, D. T. Cassidy, T. Oka, S. Miller, and J. Tennyson, *J. Mol. Spectrosc.* **145,** 222–224 (1991).
25. B. J. McCall and T. Oka, *J. Chem. Phys.* **113,** 3104–3110 (2000).
26. B. J. McCall, *Philos. Trans. R. Soc. London* **358,** 2385–2400 (2000).
27. C. S. Gudeman, M. H. Begemann, J. Pfaff, and R. J. Saykally, *Phys. Rev. Lett.* **50,** 727–31 (1983).
28. J. V. V. Kasper, C. R. Pollock, R. F. Curl, Jr., and F. K. Tittle, *Appl. Opt.* **21,** 236–247 (1982).
29. H. Adams, R. Brüggermann, P. Dietrich, D. Kirsten, H. Solka, and W. Urban, *J. Opt. Soc. Am. B* **2,** 815–827 (1985).
30. E. K. Kyrö, P. Shoja-Chaghervand, M. Eliades, and J. W. Bevan, *Rev. Sci. Instrum.* **57,** 1–5 (1986).
31. Z. S. Huang, K. W. Jucks, and R. E. Miller, *J. Phys. Chem.* **85,** 3338–3341 (1986).
32. The "étalon finder" was originally designed by W. S. Woodward, Digital Specialties, 1702 Allard Rd., Chapel Hill, NC 27514 for R. E. Miller's laboratory at the Univerisity of North Carolina at Chapel Hill. It has since been treated to a number of improvements by various groups. The present generation of the étalon finder was constructed by the James Franck Institute Electronics Shop at the University of Chicago, Chicago, IL 60637. This device inputs the étalon detector, ramp, and blank signals and outputs the ramp voltage for which the first transmission occurs as well as its intensity.
33. B. H. Pate, K. K. Lehman, and G. Scoles, *J. Chem. Phys.* **95,** 3891–3916 (1991).
34. A. S. Pine, M.I.T. Lincoln Laboratory Report NDSF/ASRA/DAR-78-24562 (1980).
35. G. Guelachvili and K. N. Rao, "Handbook of Infrared Standards II." Academic Press, Boston, 1993.
36. L. S. Rothman, C. P. Rinsland, A. Goldman, S. T. Massie, D. P. Edwards, J.-M. Flaud, A. Perrin, C. Camy-Peyret, V. Dana, J.-Y. Mandin, J. Schroeder, A. McCann, R. R. Gamache, R. B. Wattson, K. Yoshino, K. V. Chance, K. W. Jucks, L. R. Brown, V. Nemtchinov, and P. Varanasi, *J. Quant. Spectrosc. Rad. Trans.* **60,** 665–710 (1998). [HITRAN 96 Database]
37. A. Perrin, A. N'gom, V. Dana, C. Camy-Peyret, and J.-M. Flaud, *J. Mol. Spectrosc.* **122,** 365–370 (1987).
38. P. C. D. Hobbs, *Appl. Opt.* **36,** 903–920 (1997).
39. L. Neale, S. Miller, and J. Tennyson, *Astrophys. J.* **464,** 516–520 (1996).
40. L.-W. Xu, M. Rösslein, C. M. Gabrys, and T. Oka, *J. Mol. Spec.* **153,** 726–737 (1992).
41. R. Röhse, W. Kutzelnigg, R. Jaquet, and W. Klopper, *J. Chem. Phys.* **101,** 2231–2243 (1994).
42. W. A. Majewski, M. D. Marshall, A. R. W. McKellar, J. W. C. Johns, and J. K. G. Watson, *J. Mol. Spectrosc.* **122,** 341–355 (1987).
43. W. A. Majewski, A. R. W. McKellar, D. Sadovskiíí, and J. K. G. Watson, *Can. J. Phys.* **72,** 1016–1027 (1994).